JGR

Measurement and modeling of the refilling plasmasphere during 2001

J. Krall[1], J. D. Huba[1], V. K. Jordanova[2], R. E. Denton[3], T. Carranza[4], and M. B. Moldwin[4]

[1]Plasma Physics Division, Naval Research Laboratory, Washington, District of Columbia, USA, [2]Los Alamos National Laboratory, Los Alamos, New Mexico, USA, [3]Department of Physics and Astronomy, Dartmouth College, Hanover, New Hampshire, USA, [4]Department of Climate and Space Sciences and Engineering, University of Michigan, Ann Arbor, Michigan, USA

Abstract The Naval Research Laboratory SAMI3 (Sami3 is Also a Model of the Ionosphere) and the RAM-CPL (Ring current Atmosphere interaction Model-Cold PLasma) codes are used to model observed plasmasphere dynamics during 25 November 2001 to 1 December 2001 and 1–5 February 2001. Model results compare well to plasmasphere observations of electron and mass densities. Comparison of model results to refilling data and to each other shows good agreement, generally within a factor of 2. We find that SAMI3 plasmaspheric refilling rates and ion densities are sensitive to the composition and temperature of the thermosphere and exosphere, and to photoelectron heating. Results also support our previous finding that the wind-driven dynamo significantly impacts both refilling rates and plasmasphere dynamics during quiet periods.

1. Introduction

Earth's plasmasphere, a region of plasma trapped in the inner magnetosphere by closed geomagnetic field lines, is shaped by the dynamics of the magnetosphere [*Carpenter*, 1966; *Nishida*, 1966], ionosphere [*Galvan et al.*, 2008], and thermosphere [*Krall et al.*, 2014]. The plasmasphere is typically eroded during a storm, with a time scale of hours [*Goldstein et al.*, 2003], and refills during quiet times with a time scale of days [*Singh and Horwitz*, 1992]. Given its responsiveness to the magnetosphere/ionosphere/thermosphere system and its affect on electromagnetic waves and energetic particles in the inner magnetosphere [*Singh et al.*, 2011], the plasmasphere is both a marker and a component of space weather.

The purpose of this paper is to examine measurements and models of the plasmasphere during two post-storm refilling periods: 25 November 2001 to 1 December 2001 and 1–5 February 2001. In so doing we will consider plasmasphere dynamics, density, poststorm refilling, and composition, directly comparing two plasmasphere models to observations. By simulating 14 days during 2001 (including the three storm days that are not our main focus), we have model results for a large enough range of geomagnetic activity to compare to the statistical results of *Berube et al.* [2005]. To our knowledge, this is the first comparison of a first-principles global plasmasphere simulation to both mass density and electron density measurements.

Selected inputs and responses for the Earth geospace system are shown in Figure 1 for the 24 November 2001 storm and quiet refilling period and, in Figure 2, for the 31 January 2001 storm and subsequent quiet period. Shown are solar wind magnetic field components, density and velocity, extreme ultra violet (EUV) solar indices F10.7 and F10.7A, and geomagnetic indices Kp and Dst. The quiet periods of interest are 26 November 2001 to 1 December 2001 (day of year 330–336), when Kp was at or below 3 at all times and 2–5 February 2001 (day of year 33–36), when the Kp index was below 2 at all times.

Measurements of in situ plasmasphere electron density during this time are available from the Imager for Magnetopause-to-Aurora Global Exploration (IMAGE) spacecraft [*Burch*, 2000]. Measurements of mass density at the magnetic equator and at selected L shells are also available during this time. These come from the Magnetometers along the Eastern Atlantic Seaboard for Undergraduate Research and Education (MEASURE) array located along the east coast of the United States [*Berube et al.*, 2005].

Models to be used are the Naval Research Laboratory SAMI3 three-dimensional (3-D) global ionosphere/plasmasphere model [*Huba and Krall*, 2013] and the plasmasphere model used in the Ring current
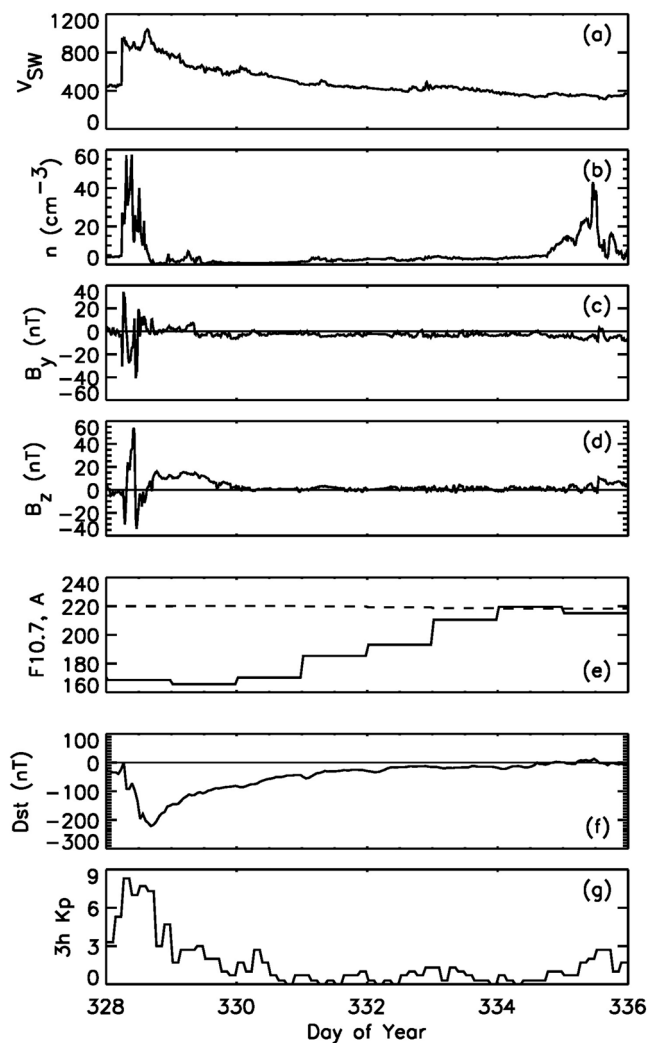
Figure 1. (a–d) Solar wind extrapolated to a position 10 R_E sunward of Earth and smoothed for the Weimer05 model: velocity (km s^{-1}), proton density, and B_y, B_z in GSM coordinates. (e) $F_{10.7}$ solar EUV index (solid line) and $F_{10.7A}$, the 80 day average (dashed). (f and g) Geomagnetic indices during the November 2001 event.

Atmosphere interaction Model-Self-Consistent Magnetic Field (RAM-SCB) [*Jordanova et al.*, 2006; *Rasmussen et al.*, 1993] referred to hereafter as RAM-CPL. We have previously simulated the February event using SAMI3 [*Krall et al.*, 2014], finding good agreement with electron density measurements. As in that previous study, we find that refilling rates vary significantly with thermosphere winds. New to this study, we find that the neutral oxygen density in the thermosphere and exosphere has a similarly strong effect on refilling. By comparing further measurements to the models and the models to each other, we will validate the models and gain further insight into plasmasphere dynamics.

2. Plasmasphere Observations

2.1. IMAGE/RPI Electron Density

Measurements of n_e in the inner magnetosphere are available from Radio Plasma Imager (RPI) instrument [*Reinisch*, 2000] on the IMAGE spacecraft, operating in the passive mode. During the November event IMAGE passes through the plasmasphere were close to 0845 and 2040 magnetic local time (MLT) at intervals of about 14 h. During the February event, passes were at MLT 0345 and 1545.

For example, Figure 3 shows n_e and IMAGE magnetic latitude MLat and MLT versus L from two such passes during November. Here open squares are points on day 330, 1649–1811 UT, after the plasmasphere was eroded by the storm on day 328, and filled squares are points on day 334, 1851–1940 UT, after 3 days of refilling
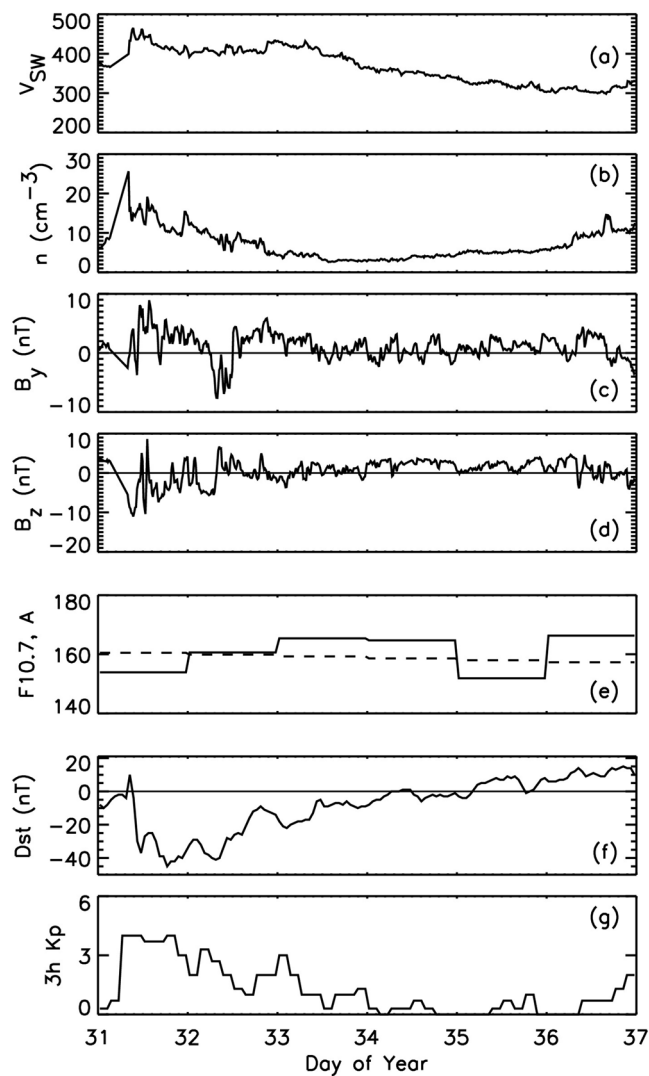
Figure 2. Same as Figure 1 but for the February 2001 event.

(curves are SAMI3 results to be discussed further below). The electron density is based either on the upper hybrid frequency or the plasma frequency found from the continuum edge [*Webb et al.*, 2007; *Denton et al.*, 2012]. Each density value is determined using an automatic algorithm. As needed, corrections are made by hand. Measurement uncertainties are less than 25% in all cases, such that error bars, if included on the plots, would be about the same size as the symbols.

2.2. MEASURE Mass Density

Measurements of equatorial mass densities are shown in Figures 4 and 5. Mass densities are computed from field line resonance (FLR) frequencies obtained from ground-based magnetometers and then numerically solved using a magnetohydrodynamic wave equation.

The meridional arrays of paired magnetometers used are from the MEASURE array located along the East Coast of the United States. The time resolution is 1 s. Data from four out of the six MEASURE magnetometers were used in this study as seen in Table 1 along with their geographical latitude and longitude, *L* shell values, and midpoint *L* shell values. The technique used for remotely sensing the mass density along closed magnetic fields in the plasmasphere involves using a pair of ground-based magnetometers to measure field line resonance frequencies [*Berube et al.*, 2005]. The method used for this study, developed by *Berube et al.* [2003], uses statistical properties from the cross phase [*Waters et al.*, 1991] and power ratio methods [*Baransky et al.*, 1985].
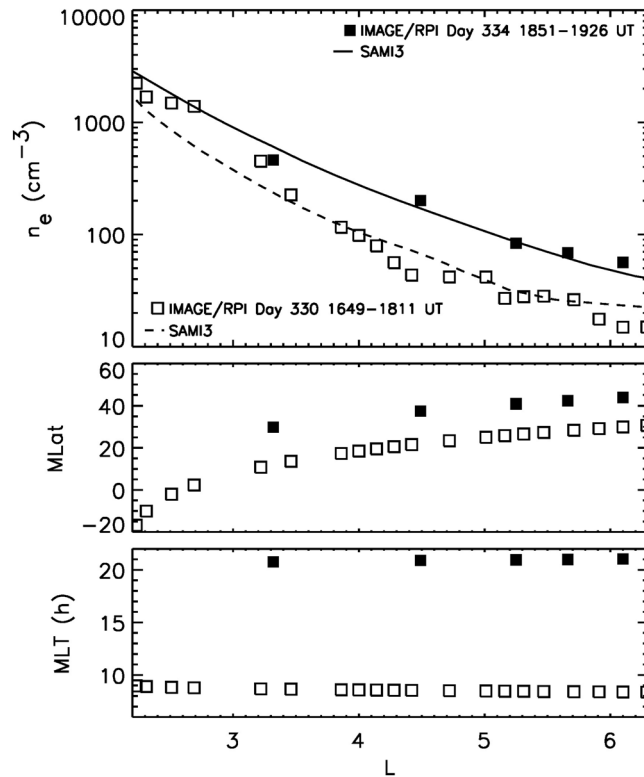
Figure 3. (top) Electron density n_e versus L from IMAGE/RPI in passive mode during 1649–1811 UT on 26 November 2001 (open squares) and during 1851–1940 UT on 30 November 2001 (filled squares). Also plotted are (middle) spacecraft magnetic latitude, MLat, and (bottom) magnetic local time, MLT. Corresponding SAMI3 electron densities are shown as curves.
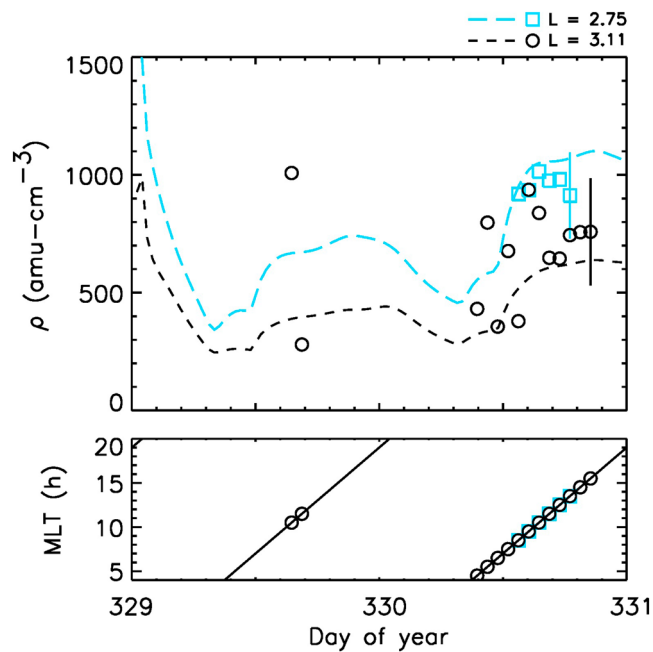

Figure 4. (top) Mass density ρ versus time from the MEASURE array, for the November event, at $L = 3.11$ (open circles) and $L = 2.75$ (open squares). Representative error bars are plotted for the rightmost points. Also plotted is the (bottom) magnetic local time MLT for each measurement. Corresponding SAMI3 mass densities are shown as curves.
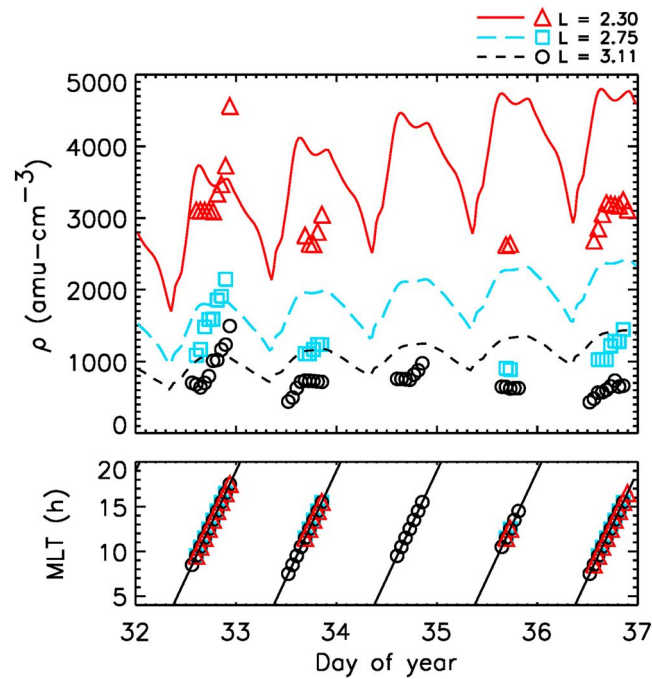
Figure 5. Same as Figure 4 but for the February 2001 event, with $L = 3.11$ (open circles), $L = 2.75$ (open squares), and $L = 2.30$ (open triangles).

Hourly average FLR frequencies were used with an uncertainty of 1.6 mHz [e.g., *Berube et al.*, 2003]. Once the FLR frequencies were obtained, the equatorial mass density was numerically calculated [*Denton et al.*, 2006] using the *Singer et al.* [1981] wave equation, solar wind parameters, the *Tsyganenko and Sitnov* [2005] model for the outer magnetic field, and the IGRF model [*Bilitza and Reinisch*, 2008] for the inner magnetic field. The frequency uncertainty leads to mass-density errors ranging from $\pm 10\%$ at $L = 2.30$ to $\pm 30\%$ at $L = 3.11$ [e.g., *Vellante and Förster*, 2006]. Representative error bars are plotted for the rightmost points in Figure 4. For further information on this method see also *Takahashi et al.* [2010].

In Figure 4, one feature that stands out is the large scatter in the $L = 3.11$ values. This suggests rapid spatial variations in density and/or composition 24–48 h after the peak of the storm. In Figure 5, we see a decrease in the measured value of ρ during refilling, which implies a reduction in number density or a change in composition over time. Based on previous measurements (e.g., *Berube et al.* [2005], discussed below), we expect the average ion mass to increase immediately following a storm and decrease thereafter.

2.3. MEASURE/IMAGE Conjunctions

Figure 6 shows average ion mass, M, determined from conjunctions of the IMAGE satellite and the MEASURE array. Included are conjunctions with $(\Delta t_{UT}^2 + \Delta T_{MLT}^2)^{1/2} < 3$ h and with IMAGE close to the magnetic equator (MLat $< 15°$). For each conjunction, RPI electron densities from an IMAGE pass are interpolated to the specified L value and extrapolated to the magnetic equator [see *Denton et al.*, 2012, equation (5)].

For these conjunctions the mean is $M = 1.1$, and the median is 1.0 for the November event. For February the mean and median are 1.4 and 1.3, respectively. These values are generally reasonable, implying a small increase in average ion mass above that of an H^+ plasma. However, the individual values are questionable;

Table 1. MEASURE Stations Used and Corresponding L Shells

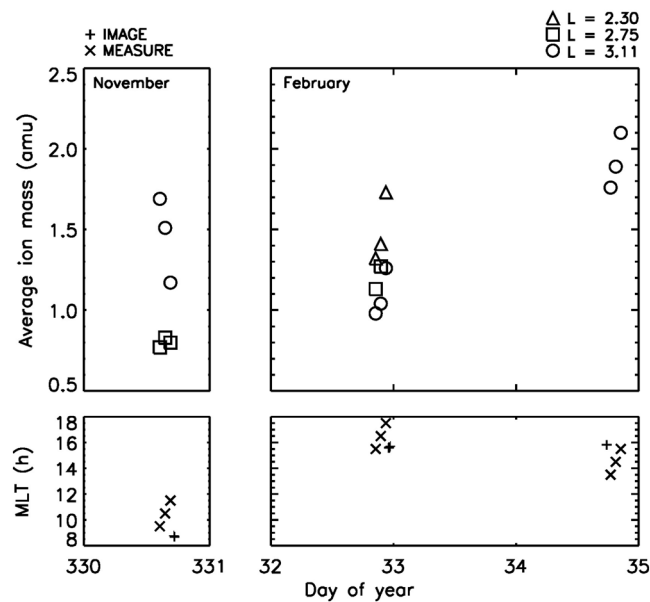| Station Name	Abbr.	Geo. Lat.	Geo. Long.	L Shell	Station Pair	Midpoint L Shell
Clarkson University	CLK	44.70°N	75.00°W	3.06		
Boston University	MSH	42.60°N	71.48°W	2.72	CLK-MSH	3.11
Applied Physics Lab	APL	39.17°N	76.88°W	2.42	MSH-APL	2.75
Dark Sky Observatory	DSO	36.25°N	81.40°W	2.18	APL-DSO	2.30

Figure 6. Average ion mass density versus universal time is shown for conjunctions of IMAGE and MEASURE measurements. Shown also are MLT values.

some values are below unity. This suggests significant variations in local electron and mass densities with time scales <3 h or spatial scales <45° longitude. We will see below that such density changes versus MLT at fixed time or versus time at a fixed MLT can be as large as a factor of 2.

The conjunction on day 34 at $L = 3.11$ is perplexing, as it suggests an increase in average ion mass during the February refilling period. Such increases have been found, such as by *Denton et al.* [2014], where an increase in O^+ was measured at geostationary orbit ($L = 6.8$). By contrast, Figure 5 shows that ρ is decreasing during refilling, when n_e is increasing. That the average ion mass for November is lower than for February is also perplexing. November has a higher EUV index, which is associated with a higher He^+ fraction. However, given that no conjunction was closer than 1.6 h (24° longitude), these M values are highly uncertain.

3. Simulation Models

3.1. SAMI3

The Naval Research Laboratory SAMI3 code [*Huba et al.*, 2008; *Huba and Krall*, 2013; *Krall and Huba*, 2013] was used in this study. SAMI3, which is based on the SAMI2 (Sami2 is Another Model of the Ionosphere) code [*Huba et al.*, 2000], includes the wind-driven dynamo electric field, solving a two-dimensional electrostatic potential equation that is based on current conservation ($\nabla \cdot \mathbf{J} = 0$). Thermospheric composition, temperature, and winds are specified, using the NRLMSISE-00 model [*Picone et al.*, 2002] for composition and temperature and either the HWM93 [*Hedin*, 1991] or the HWM14 [*Drob et al.*, 2015] empirical wind model. Initial runs were performed using HWM93; one of these is presented below for the February event. Our final run of the November event used HWM14; this is presented below.

For dynamics along field lines, SAMI3 solves the continuity and momentum equations for seven ion species. The temperature equation is solved for three atomic ion species (H^+, He^+, and O^+) and the electrons. Inclusion of He^+ and O^+ in the SAMI3 plasmasphere allows comparison to composition and mass density measurements. In the present work, we will focus on the dynamics of H^+ and He^+. *Huba et al.* [2008] provides a good description of the equation set and of the potential solver.

In the version of SAMI3 used here [*Krall et al.*, 2014], the magnetic field is a dipole aligned with Earth's spin axis and the grid is fixed relative to the Sun. In this case a constant azimuthal index corresponds to constant magnetic local time (MLT). A corotation potential is specified to account for the rotation of the Earth within this grid. In the absense of winds or magnetosphere convection, this produces an exact corotation of the ionosphere and plasmasphere.

Transport across field lines is through the $\mathbf{E} \times \mathbf{B}$ drift. These include the corotation potential, the wind-driven dynamo potential, and the high-latitude magnetospheric potential, which are simply added together. At present, the magnetospheric potential is provided by the Weimer05 [*Weimer*, 2005] empirical model, which is driven by solar wind quantities B_y, B_z, V_x, and n_p, shown in Figures 1 and 2. These solar wind data come from the OMNI data set but were smoothed using a 20 min window in preparation for use in the Weimer05 model. In these cases OMNI data are determined using measurements from the ACE [*Stone et al.*, 1998], WIND [*Harten and Clark*, 1995], and Geotail [*Frank et al.*, 1994] spacecraft for the November event and ACE and WIND for the February event.

Ionospheric processes are affected by the date, the solar irradiance indices $F_{10.7}$ and $F_{10.7A}$, and the geomagnetic index Ap, each of which are set at the beginning of each simulated day. To account for high-latitude "open" field lines, plasma densities are reduced for geocentric radius $r > 9\, R_E$.

For the November event, the simulation begins at the beginning of day 326 of 2001, in order to reduce sensitivity to initial conditions prior to the storm on day 328. Our SAMI3 simulation of the February event is described in *Krall et al.* [2014, Figures 4, 7, 8, and 10].

In this and past studies, we find that plasmasphere ion densities are sensitive to factors that do not strongly affect the ionosphere. Two examples, photoelectron heating and the atomic oxygen temperature in the exosphere, will each be considered further below. Another, the He photoionization reaction rate, was addressed by *Bailey and Sellek* [1990]. They showed that increasing the rate by a factor of 2.5 increases plasmaspheric He$^+$ density by a similar factor, bringing it in line with measurements. In recent SAMI3 modeling [*Huba and Krall*, 2013; *Krall and Huba*, 2013; *Krall et al.*, 2014], a similar increase in plasmaspheric He$^+$ density was accomplished by increasing neutral He densities, provided by the NRLMSISE-00 model in this case, by a factor of 4. For these runs we use the NRLMSISE-00 He densities, without modification. In the February case we increase He$^+$ photoproduction by a factor of 1.5. Below we will consider that this factor may not be needed; it is not included in the November case.

Preliminary modeling of the November refilling period produced rates lower than measured values by factors of 3 to 5. Noting the very high value of the 81 day average solar EUV index $218 \leq F_{10.7A} \leq 220$, we considered the possibility of inaccuracies in the NRLMSISE-00 empirical atmosphere model, which may be less reliable for such high EUV indices. We also considered using the more recent HWM14 wind model instead of HWM93.

The idea of introducing MSIS correction factors is suggested by the work of *Emmert et al.* [2014], who computed these factors for specific time periods based, in part, on measurements of satellite drag. After testing SAMI2 and SAMI3 results for sensitivity to atmospheric densities, we modified the atmosphere for the November event. The neutral oxygen density is here reduced to a factor of 0.8 and further reduced in the exosphere by effectively lowering the temperature by a factor of 0.8. In lowering the temperature, we assume an exobase at 600 km and an O density decreasing exponentially above this point based on a fixed-temperature scale height. The modified density above 600 km is $n^* = n_{600}(n/n_{600})^{T/T^*}$, where n^*, T^* are the modified values and n_{600} is the density at altitude 600 km. Comparison between empirical and measured values of density and temperature in the upper atmosphere [*Emmert et al.*, 2014] suggest that the 0.8 factor in the oxygen density is valid. The exospheric temperature reduction, however, is not presently supported by observations. We will see below that updating the wind model and lowering the atmospheric O density each increase refilling rates.

3.2. RAM-CPL

These two events were also simulated using the plasmasphere model originally developed by *Rasmussen et al.* [1993] that was later coupled with RAM-SCB [*Jordanova et al.*, 2006, 2012] and is referred to as RAM-CPL in this paper. This model calculates the thermal electron density in the equatorial plane by solving the continuity equation for the average plasma density in a flux tube (from ionosphere to conjugate ionosphere). Changes in the total flux tube content due to fluxes into or out of the tube at the northern and southern ionospheres and flux tube volume changes caused by $\mathbf{E} \times \mathbf{B}$ drifts are taken into account. In these simulations we use a dipolar magnetic field and the *Kp*-dependent convection and corotation VSMC model [*Volland*, 1973; *Stern*, 1975; *Maynard and Chen*, 1975]. The RAM-CPL runs include days 328–335 (24 November to 1 December) and days 31–36 (31 January to 5 February).

In the RAM-CPL model, refilling (or nighttime draining) is computed for each flux tube. Plasma follows the motion of individual flux tubes based on a combination of corotation and magnetospheric convection. It is
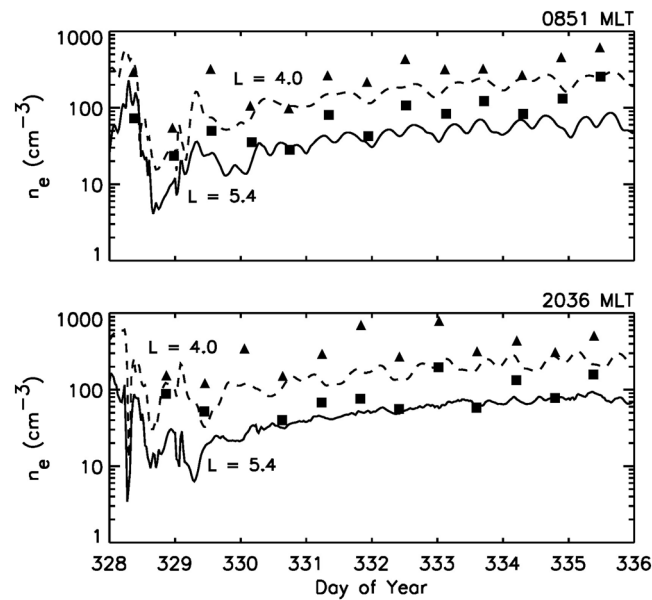
Figure 7. Electron density versus time from SAMI3 at fixed (top) 0851 MLT and (bottom) 2036 MLT and at fixed values of $L = 4.0$ (dashed curves) and 5.4 (solid curves) for the November event. Each curve has a fixed value of MLat as given in Table 1. Symbols are IMAGE/RPI measurements interpolated to $L = 4.0$ (triangles) or to $L = 5.4$ (squares) and taken at approximately fixed MLT and MLat as listed in Table 1.

assumed that thermal ion fluxes coupling the magnetosphere and the ionosphere decay exponentially with a time scale which depends on ionospheric saturation levels and on the limiting ionospheric flux. The neutral temperatures and densities required to calculate these parameters are obtained from the MSIS empirical model [*Hedin*, 1987], while the ion and electron temperatures and densities are obtained from the IRI model [*Bilitza*, 1986]. The RAM-CPL model thus depends on the relative sunspot number and the *Ap* index.

4. Results: Electron Density

Below we separately compare SAMI3 electron densities to RPI measurements, at the measured locations, and to RAM-CPL, at the magnetic equator. A key difference between SAMI3 and RAM-CPL is in electrostatic potentials, which affect the dynamics through $\mathbf{E} \times \mathbf{B}$ drifts. In SAMI3 the potential is a combination of the wind-driven dynamo, affecting low latitudes and the inner magnetosphere (approximately $L < 5$), and the solar-wind-driven Weimer potential, affecting higher latitudes and the outer magnetosphere. In RAM-CPL the *Kp*-driven VSMC potential is used. To address the difference in the Weimer05 and VSMC magnetosphere models, we have also performed SAMI3 runs using the *Kp*-driven VSMC potential, instead of Weimer05, at high latitudes.

4.1. November Event

A direct comparison of RPI passive electron density measurements and SAMI3 results is shown in Figure 3 for the November event. As discussed above, this figure shows IMAGE Mlat, MLT, and n_e versus L for two IMAGE passes (open and closed squares). Corresponding SAMI3 results are shown as curves in Figure 3 (top). SAMI3 agrees with the data for these two passes. In the eroded state, however, measured densities do not vary as smoothly as SAMI3 densities. A similar plot for the February event can be seen in Figure 7 of *Krall et al.* [2014].

Figure 7, showing SAMI3 curves at $L = 4.0$ (dashed) and 5.4 (solid) and corresponding RPI points at $L = 4.0$ (triangles) and 5.4 (squares), presents another direct comparison of the model to the data. Here each pair of points (a triangle and a square) at nearly the same time corresponds to an IMAGE/RPI pass through the plasmasphere. The two passes shown in Figure 3 correspond to the fifth pass in Figure 7 (top) and the next-to-the-last pass in Figure 7 (bottom).

Each curve in Figure 7 shows n_e from SAMI3 plotted versus time at fixed MLat and MLT coordinates approximately matching those of the IMAGE spacecraft. For example, IMAGE/RPI passes near 0845 MLT, interpolated to $L = 4.0$, have an average position of 0846 ± 0021 MLT and $15.5 \pm 4.8°$ MLat; the corresponding SAMI3 curve

Table 2. Coordinates and Electron Densities (cm^{-3}) for the November Case

L	$\langle MLT \rangle_{IMAGE/RPI}$	MLT_{SAMI3}	$\langle MLat \rangle_{IMAGE/RPI}$	$MLat_{SAMI3}$	$\langle n_e \rangle_{IMAGE/RPI}$	$\langle n_e \rangle_{SAMI3}$
4.0	0846 ± 0021	0851	15.5 ± 4.8°	14.1°	298 ± 108	162 ± 41
5.4	0847 ± 0026	0851	25.1 ± 4.0°	27.4°	85 ± 34	45 ± 11
4.0	2041 ± 0018	2036	34.0 ± 2.5°	33.2°	409 ± 209	170 ± 41
5.4	2040 ± 0025	2036	40.8 ± 2.2°	41.6°	89 ± 49	53 ± 12

is at 0852 MLT and 14.1° MLat. These coordinates are shown in Table 2 for each SAMI3 curve and corresponding RPI series of Figure 7. Similar to our previous modeling of the February event [*Krall et al.*, 2014], simulated plasmasphere densities measured at fixed MLT oscillate versus time (the 2036 MLT, $L = 5.4$ curve is an exception). In this case the oscillations do not always show a strong diurnal variation, as was seen in the *Krall et al.* [2014] runs or when modeling this same event using HWM93 winds instead of HWM14 winds. In this example, the model oscillations are not large enough to explain the variations in the data from pass to pass. Because the measurements have a low cadence, the oscillations, if present in the data, are not resolved.

Figure 7 and Table 2, where density averages are taken during the low Kp interval from 1200 UT day 330 to 0500 UT day 335, show that SAMI3 densities are generally lower than IMAGE/RPI densities. The excellent model-data agreement in Figure 3 illustrates two of the instances when density variations versus time in both SAMI3 and the data brought the two results together.

Figure 8 shows color contours of $\log_{10} n_e$, in the magnetic equatorial plane at three representative times, from the SAMI3 and RAM-CPL codes. Figure 8 (left column) shows the plasmasphere near the end of the storm. Figure 8 (middle column) is at the same time as the IMAGE/RPI data of Figure 3 (open symbols), shortly after refilling begins. Figure 8 (right column) corresponds to the later, largely refilled, state indicated in Figure 3 (closed symbols). Density profiles versus MLT at $L = 4.4$ are shown in Figure 8 (bottom row) for SAMI3 (solid curve) and RAM-CPL (dotted). We find good agreement between SAMI3 and RAM-CPL during the storm, with a plume-like feature, centered at about 1400 MLT, evident in all three plots in Figure 8 (left column).

During the quiet period the RAM-CPL plasmasphere is rounder than the SAMI3 plasmasphere. In fact it qualitatively resembles the SAMI3 plasmasphere in a run where thermospheric winds were not included in the model [see *Krall et al.*, 2014, Figure 3]. Looking at the bottom row of plots, we see that refilling is faster in RAM-CPL than in SAMI3.

4.2. February Event

A SAMI3 simulation of this event was presented in *Krall et al.* [2014], where it is the "HWM93 case" (other cases used other thermospheric wind models). Direct comparisons of SAMI3 electron densities to IMAGE/RPI data, similar to Figures 3 and 7 above, appear therein and will not be repeated here (see Figures 7 and 8, and Table 1 of that paper). However, additional comparisons to data and to the RAM-CPL code may be of interest.

Figure 9 shows color contours of n_e in the magnetic equatorial plane at three representative times for the SAMI3 and RAM-CPL codes. In Figure 9 (left column) the plasmasphere has been eroded by the storm. Figure 9 (middle column) is shortly after the storm and the Figure 9 (right column) corresponds to a later time, after 4 days of refilling. Density profiles versus MLT at $L = 4.4$ are shown in Figure 9 (bottom row).

Similar to Figure 8, SAMI3 and RAM-CPL produce similar results at the end of the storm. The agreement at this time is clear in the density profiles versus MLT (Figure 9, bottom left). At later times the two models show quite different results in terms of the plasmasphere morphology. At the end of the simulation RAM-CPL plasmasphere appears to be very round.

5. Results: Refilling

To obtain a refilling rate versus L for each event, RPI measurements of n_e during the poststorm quiet period are extrapolated to the magnetic equator as in *Denton et al.* [2012]. Results for each pass near a given MLT (a half orbit) are interpolated onto a regular L grid. The resulting time series at each L value on the grid is used to obtain a refilling rate versus L. Measured refilling rates for the two half orbits are averaged and a curve is fitted to obtain a rate versus L. For comparison, refilling rates from SAMI3 and RAM-CPL are determined from n_e averaged over longitude at the magnetic equator versus time.
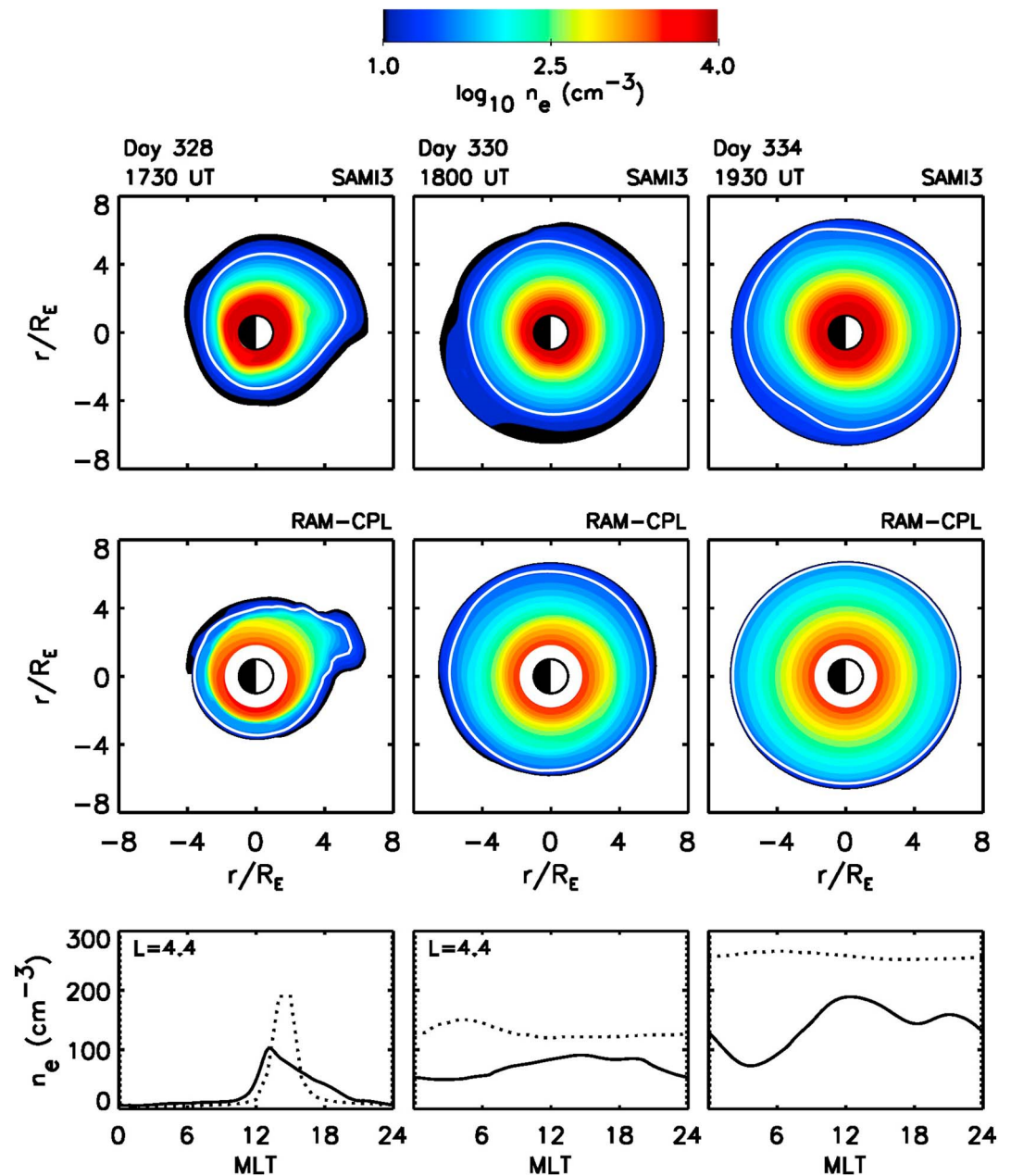
Figure 8. Color contours of n_e (log scale) in the equatorial plane from (top row) SAMI3 and (middle row) RAM-CPL at (left, middle, and right columns) three different times. Below each column is a density versus MLT profile at $L = 4.4$ for the SAMI3 contour plot (solid curve) and the RAM-CPL plot (dotted curve) in that same column. A single contour in each color plot marks constant density 30 cm^{-3}.

5.1. November Event

Based on IMAGE/RPI measurements between 1200 UT day 330 to 0500 UT day 335, the refilling rate is

$$dn_e/dt = 2.10[10^{2.88(1-L/6.8)}] \, \text{cm}^{-3}\text{d}^{-1}, \qquad (1)$$

which can also be written as $dn_e/dt = 10^{3.20-0.423L} \, \text{cm}^{-3} \, \text{d}^{-1}$. This provides a reasonable fit to measured rates for $2.5 < L < 6.5$. Equation (1) is less consistent with measured rates for $L > 6.5$, where some rates were found to be negative.

Refilling curves are shown in Figure 10 for SAMI3 and RAM-CPL. Shown is n_e averaged over longitude at the magnetic equator for $L = 4.0$ and 5.4, with solid curves for SAMI3 and dotted curves for RAM-CPL. Rates from
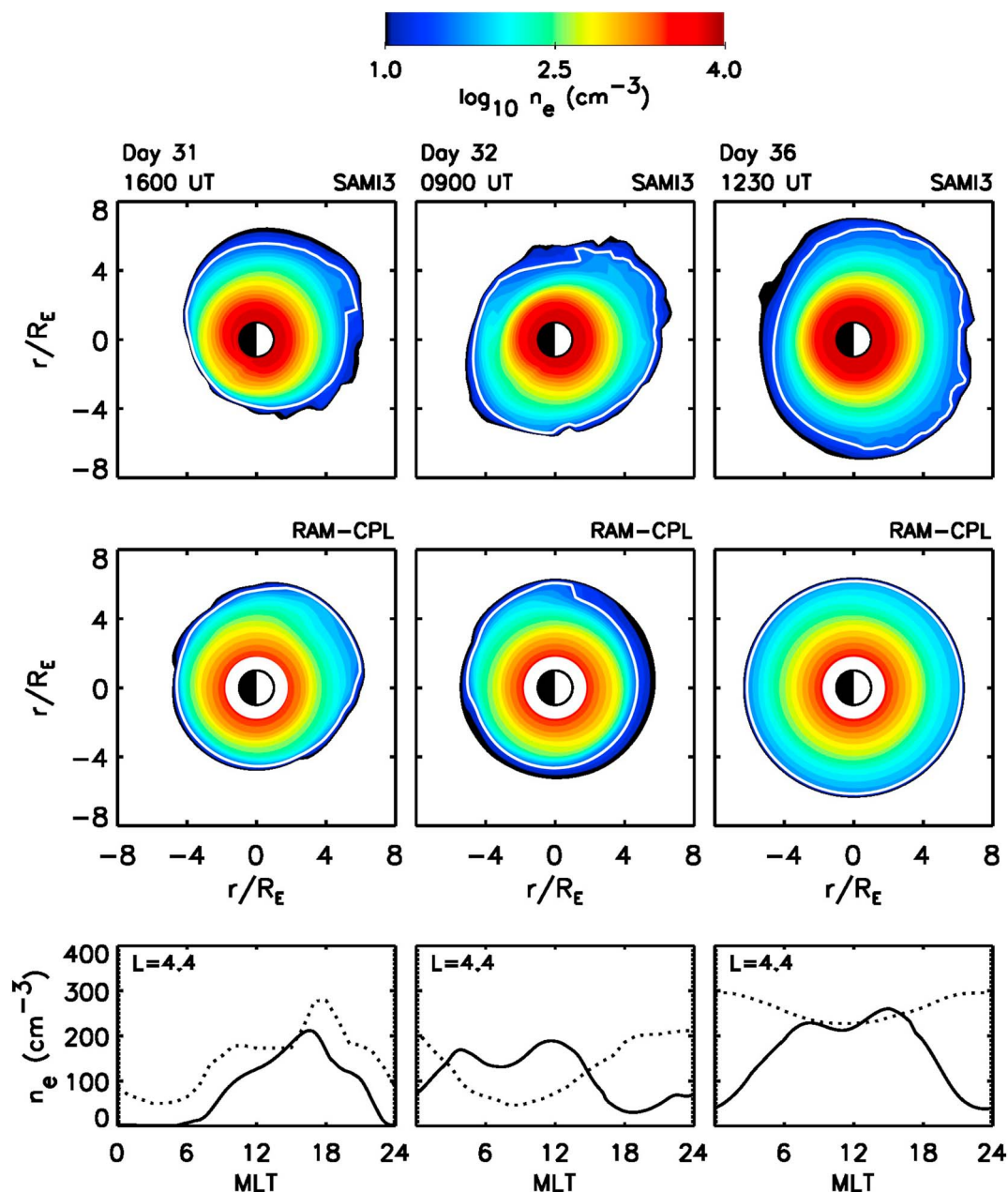
Figure 9. Same as Figure 8 but for the February event.

equation (1) are indicated by dashed lines. Refilling curves for He$^+$ from SAMI3, the long dashed curves (the He$^+$ scale is to the right), show that the He$^+$ fraction decreases from about 20% on day 330 to 12% on day 334.

Both SAMI3 and RAM-CPL curves in Figure 10 suggest a decreasing refilling rate versus time. Similarly, RPI points in Figure 7 suggest relatively fast refilling during days 330 to 333, followed by slower refilling.

Equation (1) gives refilling rates of 32.6 and 8.42 cm^{-3} d^{-1}, respectively, for $L = 4.0$ and 5.4. Corresponding rates for SAMI3, determined by a simple least squares method, are 26.5 and 7.16 cm^{-3} d^{-1}, respectively, close to the measured rates. RAM-CPL rates are 40.0 and 15.6 cm^{-3} d^{-1}, somewhat faster than measured refilling.

Refilling rates for the November event are summarized in Figure 11, where equation (1) (solid line) is plotted alongside the measured rates (squares), SAMI3 rates (black dots), and RAM-CPL rates (triangles). A vertical line on each RPI point indicates the two rates that were averaged to obtain the measured rate (because the difference in the two rates is generally larger than the uncertainty in the individual rates, each vertical line
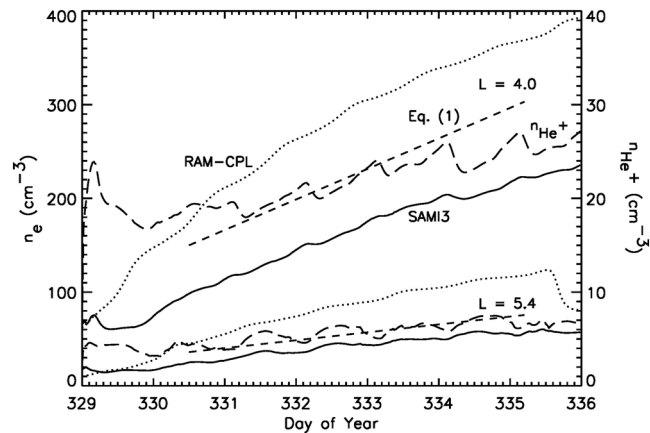
Figure 10. SAMI3 electron density (solid curves) and He$^+$ density (long dashed curves; scale to the right) averaged over longitude in the equatorial plane plotted versus time for $L = 4.0$ and 5.4 for the November event. Electron density from RAM-CPL is shown as dotted curves. Dashed lines indicate rates from equation (1).

serves as an error bar). Both SAMI3 and RAM-CPL agree nicely with the data. For $L > 5$, RAM-CPL rates are about a factor of 2 larger than SAMI3 rates. Here measured rates lie between the two model results with the two measured results at each L also differing by a factor of about 2 in some instances.

Similar to *Krall et al.* [2014], refilling rates varied with the wind model used, with HWM93 giving the slowest refilling. As discussed in section 3.1 above, modifications to the NRLMSISE-00 thermosphere and exosphere had the effect of increasing refilling rates. For comparison, results from SAMI3 with HWM93 (versus HWM14) and/or unmodified MSIS are also shown in Figure 11. The winds and the atmospheric O density profile have similar effects, each reducing refilling rates by 30–40%. The combined effect (red dots) is a reduction of about 65%.

5.2. February Event

As with equation (1), and as reported by *Krall et al.* [2014], a refilling rate was determined for the February event, based on RPI n_e measurements during the low Kp interval from 0600 UT day 33 to 0900 UT day 36:

$$dn_e/dt = 3.81(6.8/L)^{4.94} \mathrm{cm}^{-3} \mathrm{d}^{-1}. \tag{2}$$

Example refilling curves and rates from equation (2) are shown in Figure 12. Whereas equation (2) gives 55.3 and 12.1 cm^{-3} d^{-1}, respectively, at $L = 4.0$ and 5.4, SAMI3 gives 37.3 and 10.4 cm^{-3} d^{-1} and RAM-CPL gives 29.2 and 19.0 cm^{-3} d^{-1}. Figure 12 indicates a SAMI3 He$^+$ fraction at $L = 4$ that is nearly constant at 7%.
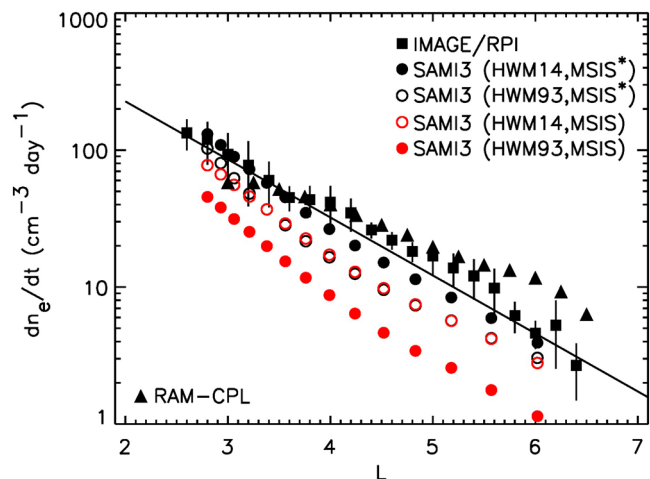

Figure 11. Refilling rates (squares) versus L based on IMAGE/RPI measurements for the November event; the solid line is equation (1). Each vertical line indicates the two refilling rates that were averaged to obtain the point. Black dots indicate rates from SAMI3 with HWM14 winds and a modified thermosphere. Triangles are RAM-CPL rates. Additional SAMI3 points show results with HWM93 winds and/or the unmodified MSIS thermosphere.
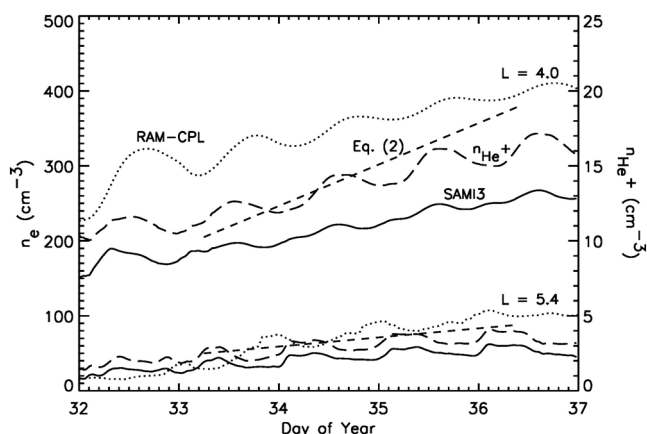
Figure 12. Same as Figure 10 but for the February event. Here dashed lines show rates from equation (2).

Results are summarized in Figure 13, where IMAGE/RPI refilling rates at each L value are shown as squares alongside SAMI3 rates (dots) and RAM-CPL rates (triangles). As in Figure 11, the SAMI3 rates are lower than RPI rates.

At low L, RAM-CPL rates differ notably from measurements. In this mild storm (see Figure 2) both RAM-CPL and SAMI3 show little erosion within $L = 4$, whereas the data indicate erosion down to about $L = 3.3$ [see *Krall et al.*, 2014, Figure 6]. This suggests that the models do not capture the full effect of the geomagnetic storm on the plasmasphere. Accordingly, discrepancies in the refilling rates are largest for $L < 4$, with RAM-CPL rates being negligible. Between $L = 4.2$ and 5.5, however, RAM-CPL agrees quite well with the measurements.

6. Results: Composition

6.1. November Event

Figure 14 shows color contours of the SAMI3 H^+ and He^+ ion densities in the magnetic equatorial plane at the same times as in Figure 8. Color contours of the He^+ fraction (Figure 14, bottom row) show that the He^+ composition is 10–20% over much of the plasmasphere during refilling (Figures 14 (middle column) and 14 (right column)), consistent with Figure 10.

Figure 14 (bottom row), particularly the left and middle panels, suggests that the H^+ and He^+ components of the refilling plasmasphere differ in structure. Because a plume-like feature on day 328 is more in evidence for H^+ than for He^+, this figure suggests that H^+ is more strongly affected by geomagnetic storms than He^+, as found in Dynamics Explorer 1 satellite data by *Newberry et al.* [1989]. However, because the n_{H^+} and n_{He^+} contours are on the same scale, some details are lost from the n_{He^+} plot. This will be discussed further below.
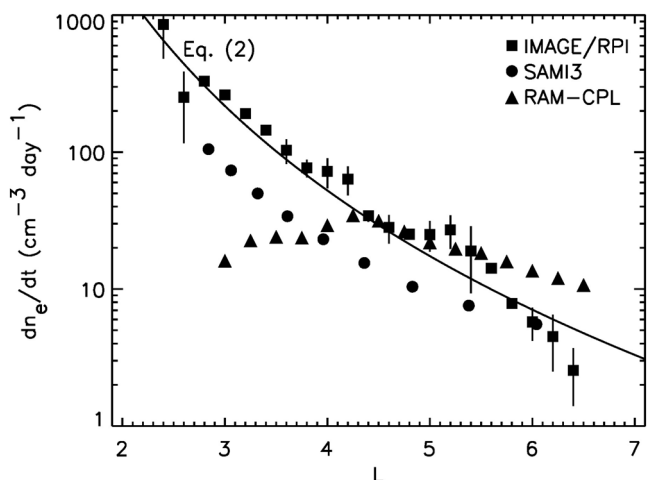

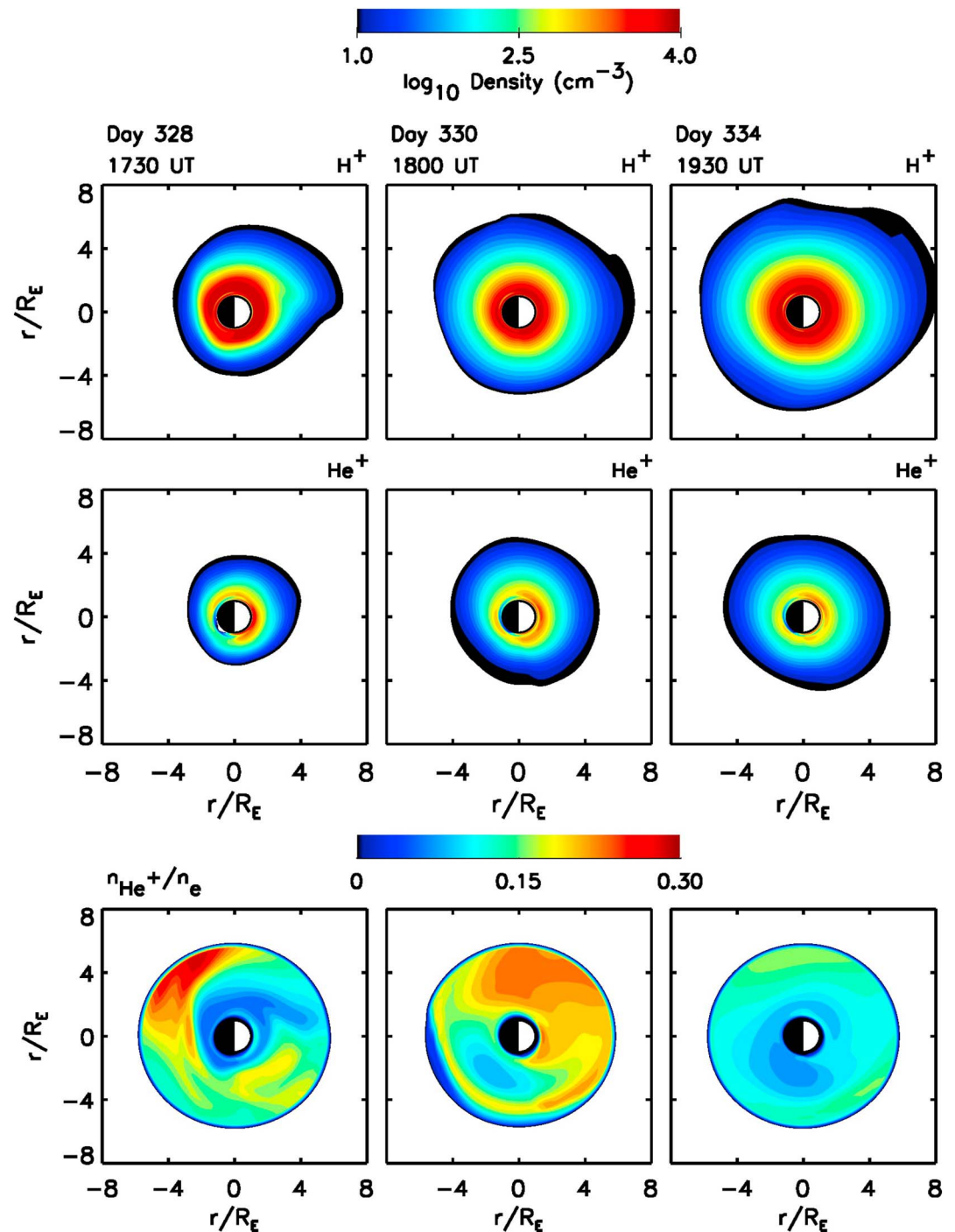**Figure 13.** Same as Figure 11 but for the February event. Winds in this case are from HWM93.

Figure 14. Color contours of (top row) H$^+$ density and (middle row) He$^+$ density at (left, middle, and right columns) three different times in November. (bottom row) Color contours of the He$^+$ fraction.

During the storm (Figure 14, left column) there is a high fraction of He$^+$ outside of the apparent plasmapause. This is suggestive of the heavy ion torus that is seen in the inner magnetosphere during strong storms [*Berube et al.*, 2005]. What is generally observed, in fact, is an O$^+$ torus, which is also present in the simulation. However, modeling the O$^+$ torus is beyond the scope of the current work.

Mass density ρ from SAMI3 is compared to the MEASURE measurements in Figure 4. The agreement is quite good. Variations versus local time on day 330 are reproduced, to some degree. In this figure, 30–50% of the SAMI3 mass density is contributed by He$^+$ and only 3–5% by O$^+$.
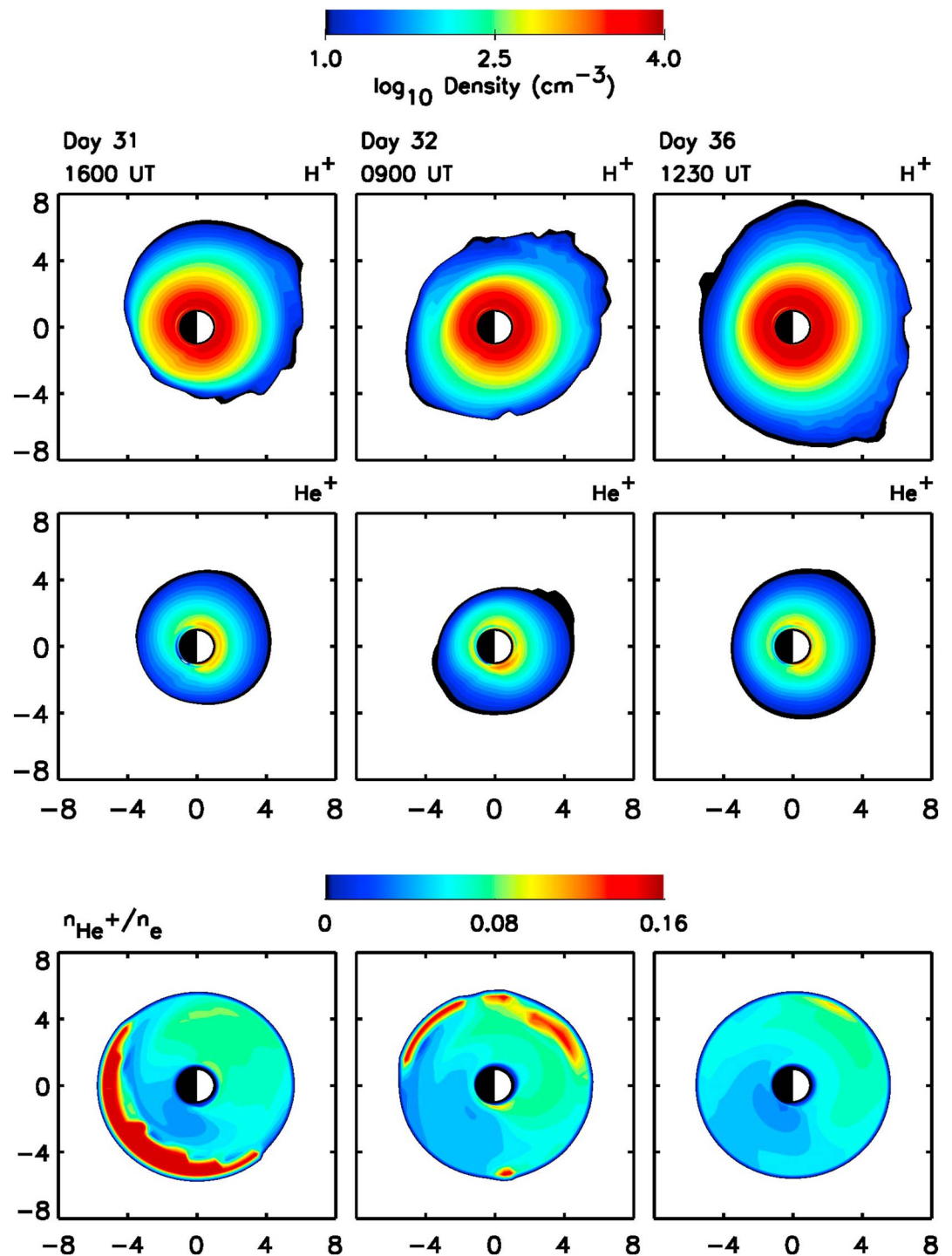
Figure 15. Same as Figure 14 but for the February event.

6.2. February Event

Figure 15 shows color contours of the H$^+$ and He$^+$ ion densities and He$^+$ composition in the magnetic equatorial plane at the same times as in Figure 9. Similar to the corresponding November result, plots of the He$^+$ fraction (Figure 15, bottom row) show some evidence of a heavy ion torus, especially during and after the storm. During refilling the He$^+$ fraction is 4–8% over most of the plasmasphere.

Figure 15 suggests that, while the He$^+$ near Earth is strongly influenced by photoionization in a spatial pattern fixed relative to the Earth-Sun line (the He$^+$ fraction for $L < 2$ is strongest during the day and weakest just
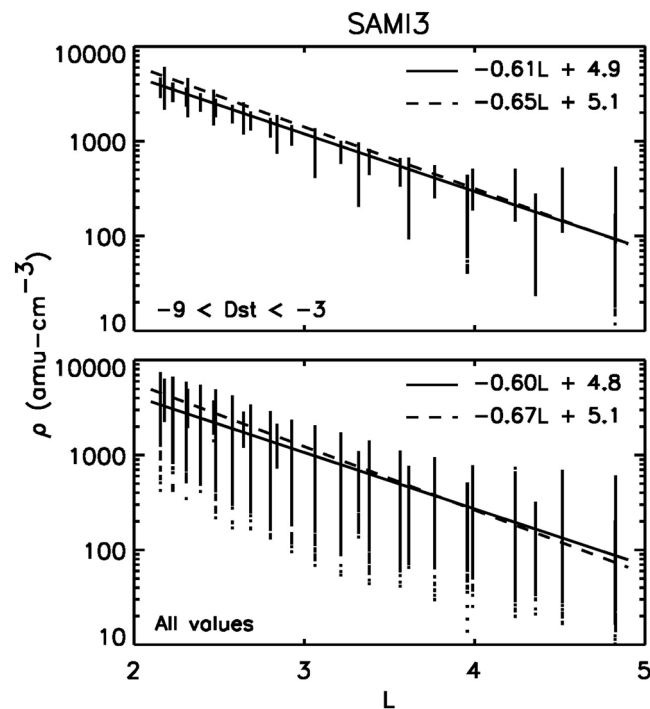
Figure 16. Scatter plot of SAMI3 ρ versus L in the dayside equatorial plane for (top) quiet times and (bottom) all times. An exponential fit to each set of points is shown as a solid line, with the exponent formula given. Dashed lines are corresponding results from *Berube et al.* [2005], based on measured values.

before dawn), the He$^+$ component at higher L values appears to be corotating with Earth. For example, the red area on day 31, 1600 UT (Figure 15, bottom left), rotates by about 17 h in local time by the time of the day 32, 0900 UT plot (Figure 15, bottom middle).

SAMI3 ρ values are compared to MEASURE data in Figure 5. The agreement is quite good on day 32, but SAMI3 values slowly diverge from measured values thereafter. On day 36 some values differ by more than a factor of 2. As noted above, measured decreases in ρ during refilling suggest a change in composition. The SAMI3 values, by contrast, do not reproduce this effect. Here 15–20% of the SAMI3 mass density is contributed by He$^+$ and 0–9% by O$^+$.

7. Results: Mass and Electron Density Versus *L*

We now compare SAMI3 results to *Berube et al.* [2005], who compiled 5200 h of mass density measurements during 1999–2001, using the MEASURE magnetometer array for $2 < L < 3.2$. These data include 1098 h during quiet times, defined as $-9 < Dst < -3$ nT and 266 h during disturbed times, $Dst < -100$ nT. Almost all measurements (95%) were taken on the dayside, 0600–1800 MLT. SAMI3 simulations of the two periods shown in Figures 1 and 2 produced output at 634 unique UT values, 82 during quiet times and 53 during disturbed times. The similarity of the total:quiet:disturbed ratios in these two distributions of samples, 520:110:27 and 634:82:53, suggests that comparisons would be valid, with adjustments in the weighting given to the model outputs to bring these ratios into line with the measured ratios.

We will compare model results with those of *Berube et al.* [2005] for quiet times and for the entire sample, but not for disturbed times, where our model sample sizes are much smaller. Disturbed times are not the focus of these SAMI3 and RAM-CPL simulations, which do not include, for example, a self-consistent model of the storm time magnetospheric convection potential. In other studies, this potential has been included in SAMI3 [*Huba and Sazykin*, 2014] and RAM-SCB [*Chen et al.*, 2010].

Berube et al. [2005] find that the average mass density of the dayside plasmasphere in the equatorial plane, based on all samples, is $\rho_{eq}(L) = 10^{-0.67L+5.1}$. The corresponding SAMI3 result, $\rho_{eq}(L) = 10^{-0.60L+4.8}$, is in good agreement, as shown in Figure 16 (bottom). Plotted are SAMI3 mass density points on a log scale along with a least squares fit to the log of the average density versus L for quiet (Figure 16, top) and all times
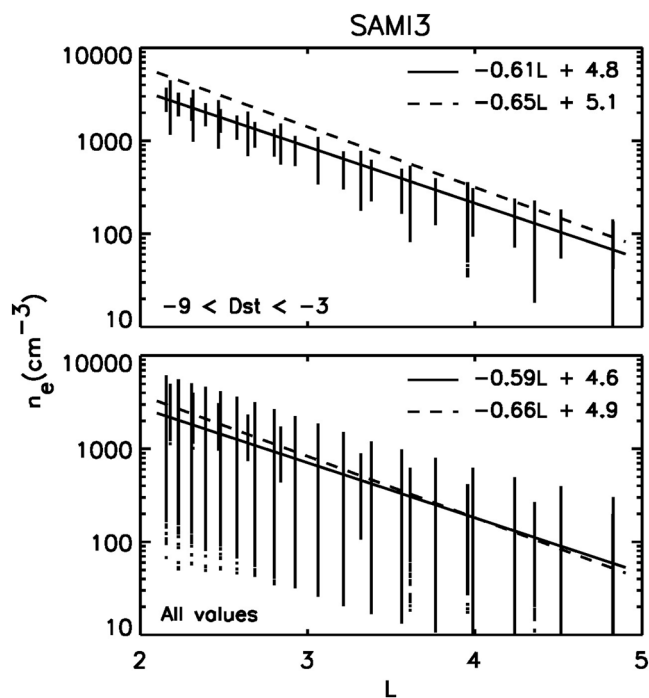
Figure 17. Same as in Figure 16 but for n_e versus L.

(Figure 16,bottom). In each case the *Berube et al.* [2005] result is shown as a dashed line. The discrete distribution of SAMI3 points versus L is a result of the SAMI3 numerical grid (the grid differs slightly between the November and February runs).

Berube et al. [2005] similarly produced profiles of electron density versus L, based on IMAGE/RPI passive-mode measurements between May 2000 and May 2001. These data include only measurements within 20° of the magnetic equator, but do include all available MLT values. In this case the total:quiet:disturbed sample ratios
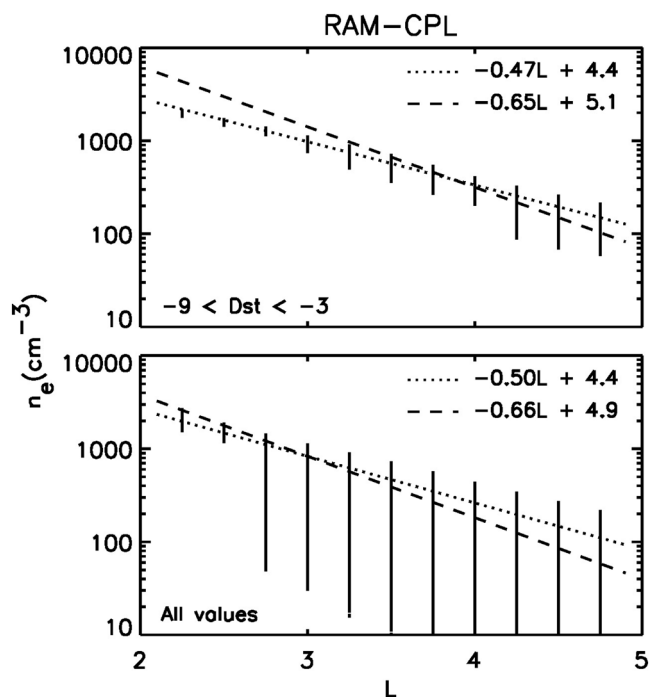

Figure 18. Same as in Figure 17 but with dotted lines showing exponential fits to results from the RAM-CPL model.

were not reported so we simply use all data points. The SAMI3 results (solid lines) are shown in Figure 17, along with the *Berube et al.* [2005] results (dashed lines), for quiet (Figure 17, top) and all times (Figure 17, bottom). Results are in good agreement. As in Figure 7, the quiet-time SAMI n_e values are lower than observed, with the discrepancy being less than a factor of 2.

For comparison we produce the equivalent $n_e(L)$ plot for the RAM model where the sample distribution is 661:86:53 (total:quiet:disturbed). Figure 18 shows a linear fit to average n_e versus L plotted as a dotted line for quiet (Figure 18, top) and all times (Figure 18, bottom). The RAM profiles vary less rapidly with L than observed, but the discrepancy in n_e values never exceeds a factor of 2.

8. Discussion

By comparing data to two different plasmasphere models and the models to each other, we compare and contrast three realizations of the quiet-time plasmasphere, each with known limitations. Of interest are the questions raised by the many small discrepancies between data and the models, and the models and each other.

8.1. Influence of the Model Thermosphere and Exosphere

In this study, SAMI3 reproduced the experimental finding that the refilling rate tends to fall with increasing solar activity. However, preliminary runs showed an overly strong rate reduction, with very low densities and refilling rates for the November event ($F_{10.7A} \approx 220$) versus the February event ($F_{10.7A} \approx 160$).

The tendency of H^+ refilling rates to fall with increasing solar activity has been attributed to reduced neutral H in the H^+ source region, where H^+ is produced via a charge-exchange reaction with O^+ [*Richards and Torr*, 1985]. Noting that the topside ionosphere O^+ density increases with solar activity, *Krall et al.* [2008] speculated that, because O^+ acts as a diffusive barrier to H^+ upflow [*Lemaire and Gringauz*, 1998], the increase in O^+ with sunspot number might explain a corresponding reduction in H^+ refilling rates.

To address too low model refilling rates at very high solar activity, we explored three possibilities. We considered that there might be more photoelectron heating in the topside ionosphere than is accounted for in our model. However, adding more heating produced a heavy-ion population in excess of the observations. This will be further discussed in section 8.3 below. Another possibility is that results might be sensitive to the density, composition, and temperature of the thermosphere and exosphere. A third is that updating the wind model from HWM93 to HWM14 might make a difference.

After further simulations, we modeled the November event with an atmosphere where the neutral oxygen density n_O and exospheric temperature $T_{O,exo}$ were each reduced by a factor of 0.8. With these modifications to the NLRMSISE-00 atmosphere (see section 3.1 for further detail), we modeled the event 4 times: with HWM93 versus HWM14 and with modified versus unmodified NRLMSISE-00 values.

Observations of atmospheric mass density suggest that applying the 20% density reduction to the NRLMSISE-00 model is physically sound [*Emmert et al.*, 2014]. Density fluctuations of $-0.3 < \ln(\rho/\rho_{MSIS}) < 0.2$ are common. Figure 17 of *Emmert et al.* [2014] shows a downward fluctuation in the 61 day average ρ/ρ_{MSIS} in late 2001. However, these measurements do not lend observational support to our modification of $T_{O,exo}$. Reducing $T_{O,exo}$ has the effect of making n_O, and n_{O^+}, fall off more rapidly above an assumed exospheric base of 600 km.

Both modifications reduce the degree to which O^+ impedes the diffusion of H^+ into the plasmasphere. This reduction in the well-known O^+ diffusive barrier also increased the He^+ fraction by a few percent, calling into question the need to artificially increase He^+ photoproduction as done in the February simulation and in *Bailey and Sellek* [1990]. In any case these modifications increased refilling rates and resulting electron densities by about 60%. The sensitivity of the plasmasphere density, composition, and refilling rates to conditions in the thermosphere and exosphere merits further study.

The impact of thermosphere winds on refilling rates has already been explored in *Krall et al.* [2014, Figure 9]. In the previous work, inclusion of HWM07 winds [*Drob et al.*, 2008] or TIMEGCM (Thermosphere Ionosphere Mesosphere Electrodynamics General Circulation Model) composition and winds [*Roble and Ridley*, 1994; *Crowley et al.*, 1999] in place of the HWM93 winds used in our present modeling of the February event was shown to increase refilling by as much as a factor of 2. This effect is confirmed in Figure 11, where refilling rates for the November event are compared for SAMI3 with HWM93 versus HWM14 winds. With HWM14,

refilling rates are larger and agreement with data (and with RAM-CPL) is excellent. It is reasonable to suppose that using HWM14 winds instead of HWM93 winds would have a similar effect on our February SAMI3 results.

8.2. Electron Density

Krall et al. [2014] showed that, without the influence of thermospheric winds on the potential, the model quiet-time plasmasphere is round. This effect is effectively reproduced by the RAM-CPL code in Figures 8 and 9. The round RAM-CPL plasmasphere in the right column of each of these figures resembles the SAMI3 plasmasphere with no winds [see *Krall et al.*, 2014, Figure 12]. Because RAM-CPL does not include wind-driven dynamo electric fields, this result was not unexpected.

As noted above, SAMI3 and RAM-CPL use different magnetospheric potential models, with SAMI3 using Weimer05 and RAM-CPL using VSMC. Additional SAMI3 simulations of the November event, with the *Kp*-driven VSMC potential used instead of the Weimer05 model, were also performed. In general, the agreement between SAMI3 and RAM-CPL was improved when the VSMC potential was used. During quiet refilling, the SAMI3/VSMC model plasmasphere was somewhat rounder than the SAMI3/Weimer05 plasmasphere.

This suggests that models of the inner magnetosphere, such as RAM-CPL, might benefit by including a model of the wind-driven dynamo. Assuming that this is the case, it would be interesting to know the circumstances in which the wind-driven dynamo significantly affects dynamics in the inner magnetosphere. It is expected, but not certain, that this field would be overwhelmed by the magnetospheric convection potential during storms. However, the wind-driven dynamo might exert influences on the plasmasphere that vary with season, with solar cycle, or even on much shorter time scales. Plots of F layer $\mathbf{E} \times \mathbf{B}$ drifts [*Scherliess and Fejer*, 1999] show strong scatter, for example. The degree to which the thermosphere introduces significant day-to-day variability into the plasmasphere is not yet known.

8.3. Refilling: Modeling

Comparisons between older and newer models are useful to provide context for newer models and to suggest model updates. Both SAMI3 and RAM-CPL generally agree with measured refilling rates to within a factor of 2, and are often much closer. Given the degree of scatter in previous refilling measurements [see *Denton et al.*, 2012, Figure 1], this seems like a reasonable result. However, it should eventually be possible to obtain better agreement for a specific well-measured event. Further, lower-than-measured SAMI3 rates sometimes differ from higher-than-measured RAM-CPL rates by as much as a factor of 4. Empirical parameters that effect refilling in RAM-CPL have been well-tested against previous poststorm periods at geosynchronous orbit [*Lambour et al.*, 1997]. In the present case we add to previous validation studies by performing data-model comparisons at a range of L values.

As discussed in section 3.1 above, we varied SAMI3 parameters affecting He^+ densities and electron heating in order to better model the electron and mass densities. We find that adding He^+ production, by either increasing the production rate [see also *Bailey and Sellek*, 1990] of the neutral He density, increased refilling rates. Comparing otherwise identical SAMI3 runs, we found that variations of up to a factor of 4 in specified neutral He density or of up to a factor of 2 in He^+ photoproduction rates affect refilling rates by only a few percent.

One source of uncertainty in the modeling is the photoelectron heating, an affect that is computed in SAMI3. In previous runs, we have found that SAMI3 densities and refilling rates are sensitive to the degree of photoelectron heating. This can be seen in *Huba and Krall* [2013] and *Krall and Huba* [2013], where photoelectron heating was reduced by an ad hoc factor of 0.15 relative to the usual model [see *Huba et al.*, 2000, section 3.5] and the resulting densities and refilling rates are somewhat low. Without the factor of 0.15, we find that the agreement improves, but refilling rates are still somewhat low [*Krall et al.*, 2014]. *Varney et al.* [2012] created a more sophisticated photoelectron model for SAMI2, but that is numerically expensive and has not been introduced into SAMI3.

In this study we performed additional SAMI3 runs with photoelectron heating increased by 1.5 relative to the results shown above. We found that refilling rates increase approximately linearly with photoelectron heating. The additional heating, however, produced significant additional O^+ ions such that model mass densities were over twice the measured values. In any case we plan to update the photoelectron model so as to better approximate the *Varney et al.* [2012] results.

Another interesting result is the observation of refilling for $L < 4$ in the February case, Figure 13, that is reproduced by SAMI3 but not by RAM-CPL (in the November case, this discrepancy between SAMI3 and RAM-CPL

at low L is not apparent). The reduction of densities inside of the poststorm plasmapause location, leading to subsequent refilling, is a common feature [*Park*, 1973]. However, the cause of the storm time density reduction at low L values is not clear. Key differences between these SAMI3 and RAM-CPL runs are the inclusion of the Weimer05 potential in SAMI3 versus the VSMC potential in RAM-CPL and the inclusion of the wind-driven dynamo in SAMI3. This issue merits further study.

8.4. Refilling: Physics

In this study we consider two periods of refilling during 2001, near the maximum of the solar cycle. These events illustrate the tendency of refilling rates to fall with increasing solar activity [*Su et al.*, 2001]. This can be seen by comparing Figure 13 ($F_{10.7A} = 160$) to the lower refilling rates of Figure 11 ($F_{10.7A} = 220$). Here and in previous modeling [*Krall et al.*, 2008], we attribute this decrease to the tendency of O^+ to retard the diffusion of H^+ out of the topside ionosphere. For example, *Lockwood* [1984] showed that auroral outflows of energetic O^+ are sensitive to both the density and scale height of thermal O^+.

As in *Krall et al.* [2014], refilling rates are affected by winds. Again, we find that higher refilling rates are associated with high total electron content (TEC), the vertically integrated electron density. In *Krall et al.* [2014], we showed that wind-driven vertical/meridional $\mathbf{E} \times \mathbf{B}$ drifts can raise or lower the ionosphere, raising or lowering TEC at the high-latitude (about 60°) footpoints of plasmaspheric field lines of interest. Plots of TEC for SAMI3 using HWM14 versus HWM93 winds (not shown) verify that HWM14 produces higher TEC at high latitudes.

Given the association of high refilling rates with high TEC, one might expect the high TEC associated with high solar activity to cause high refilling rates. Instead, the decreased refilling associated with increased solar activity is a matter of the diffusive barrier effect (the atmosphere and the ionosphere are "puffed up" during solar maximum) dominating the TEC effect. The runs where we reduced both the density of atomic O and its exosphere temperature (so the O density falls more rapidly with height), are consistent with this interpretation: Despite the fact that the lower O density is associated with a weaker ionosphere (lower TEC) the lowered diffusive barrier increases refilling rates.

It is important to recognize that we cannot get any result we desire from these models simply by changing input values. For example, adding heat to the system via the photoelectron heating function increases refilling but at the expense of adding too many heavy ions to the plasmasphere. With respect to our modifications to the NRLMSISE-00 atmosphere, we are constrained by measured n_O and inferred T_{exo} [*Emmert et al.*, 2014]. Further, this is only a single result at a particularly high level of solar activity ($F_{10.7A} = 220$). Studies of this effect, including a wider range of solar activity, are clearly needed.

Our finding that RAM-CPL refilling rates are often higher than observed calls into question the source fluxes used to compute flux tube electron content. *Rasmussen et al.* [1993] describe both the flux tube content model equations, which are essentially the same equations solved in RAM-CPL, and an empirical determination of flux tube saturation times (see Figure 7 therein). At the December solstice during solar maximum, the empirical saturation time is about 12 days and is approximately constant versus L for $3 < L < 5.5$. The model refilling curves in Figures 10 and 12 are consistent with this in the sense that they do not saturate during the 5–6 day quiet period available in each case and in the sense that each refilling curve is clearly approaching saturation, with the possible exception of the $L = 4$ curves in Figure 12.

An extensive study by *Denton et al.* [2012], using IMAGE/RPI plasmasphere density measurements during 2001–2006, provides context for the present work. Specifically, *Denton et al.* [2012, Figure 1] found refilling rates lower than those reported from numerous previous measurements. We hypothesize that, prior to the IMAGE mission, reported measurements of individual events focused on cases where refilling was clearly evident. That is, previous studies of individual refilling events may have been biased in favor of events with relatively high refilling rates.

Refilling rates for these two specific periods are lower still. At $L = 4$, for example, the measured refilling rate is 32.6 cm^{-3} d^{-1} for the November event and 37.3 cm^{-3} d^{-1} for the February event. Both values are lower than 43.7 cm^{-3} d^{-1}, the median value based on all 34 quiet periods identified within the IMAGE/RPI data stream [see *Denton et al.*, 2012, equation (9)]. This is not surprising, given the high $F_{10.7}$ values during our two events.

8.5. Composition

We find model He$^+$ fractions consistent with typical values of about 1–4% for low to moderate solar activity and 10–15% for high solar activity [*Newberry et al.*, 1989; *Krall et al.*, 2008]. However, other studies have found

He$^+$ fractions of 25% [*Craven et al.*, 1997] or higher [*Berube et al.*, 2005]. These EUV indices are unusually high, with $F_{10.7A} = 220$ throughout the November event (Figure 1e). In the quiet-time plasmasphere, high $F_{10.7}$ is generally associated with a high He$^+$ fraction, because He$^+$ is directly created from He via photoionization.

SAMI3 reproduced measured poststorm mass densities for both events, as seen in Figures 4 and 5. In the February event, however, modeled mass densities increase while measured mass densities are flat or decreasing during refilling. It is perhaps notable that the artificial increase in the He photoionization reaction rate that was used by *Bailey and Sellek* [1990] in their modeling of the plasmasphere and in some of our work is apparently not needed. It is not included in the November event, where agreement with data is excellent but was included in the February event. In our February case, the reaction rate was increased by 50% and model mass densities were often higher than measured.

Missing in these simulations are high-latitude outflows of energized ions, which could introduce additional O$^+$ (and other ions) into the system via magnetospheric convection ($\mathbf{E} \times \mathbf{B}$ drifts) from high to low L values in the midnight sector. Energized heavy ions might precipitate out of the plasmasphere after the storm, explaining the observational result of Figure 5. Here the mass density decreases or remains level while the electron density increases.

Similar to Figure 7, Figure 17 shows reduced model n_e relative to quiet-time observations. While Figure 17 (top) may indicate needed model improvements, as discussed above, it may also be affected by differences between the model and data sampling. Where the data were taken over a long period of time, our model results focus specifically on poststorm refilling periods during which densities may be lower than average.

Notable is the fact that the H$^+$ component of the plasmasphere appears to be more structured than the He$^+$ component. This can be seen in Figure 14 (left column), where the plume appears to be stronger in the H$^+$ contour plot. This artifact comes about because the H$^+$ and He$^+$ plots are on the same scale. In Figure 14 (bottom left), a plume-shaped structure is clearly visible as a region of low n_{He^+}/n_e. The significance of this plot is not clear, but it does suggest that our understanding of plasmaspheric composition and density structure is incomplete. For example, in situ n_e measurements of plumes from geostationary satellites ($L = 6.6$) have been interpreted as residual plumes wrapped all the way around Earth as they orbit during a poststorm quiet period [*Goldstein et al.*, 2014]. By contrast EUV images of the He$^+$ component suggest plumes that are less structured and do not extend as far around Earth [*Garcia et al.*, 2003].

9. Conclusion

We have presented the first comparison of a first-principles global plasmasphere simulation to both mass and electron density measurements, using the SAMI3 and RAM-CPL models. Results are encouraging, with models generally agreeing with data to within a factor of 2. These results generally serve to validate the models and to further support recent findings.

In particular, we again find that the thermospheric wind-driven dynamo affects the plasmasphere during geomagnetically quiet times. The most pronounced effect in this study was a 60% increase in refilling rates when HWM14 winds were used in place of HWM93 winds. Winds also introduce plasmaspheric density variations that corotate with Earth. As a result, measurements at fixed magnetic local time, such as IMAGE/RPI n_e measurements, should oscillate versus universal time. IMAGE/RPI n_e measurements show variation of the expected amplitude for the February event, but variations in the data are larger than would be expected based on our modeling of the November event. The oscillations, if present in the data, are not resolved.

Among our new findings is the sensitivity of refilling rates and resulting n_e to the density and composition of the thermosphere and exosphere. In particular, reducing the density and/or the exospheric temperature of neutral oxygen increases refilling rates. Similar to the wind effect, a 20% decrease in both the O density and O exosphere temperature produced a 60% increase in refilling rates. The sensitivity of refilling rates to O density in the thermosphere and exosphere will be studied further.

We also examined the sensitivity of both the refilling rate and the O$^+$ fraction to the degree of photoelectron heating. In the February case, for example, we may have refilling rates that are too low in order to avoid O$^+$ densities that are too high. A planned update of our photoelectron heating model might change this relationship.

Another possibility is that improvements to the model might affect the refilling rate without affecting the composition. One such change would be a two-stream treatment of H^+, the main component of refilling, as in *Rasmussen and Schunk* [1988]. In a two-stream treatment, H^+ ions entering the plasmasphere from the Northern and Southern Hemispheres pass through each other near the magnetic equator, avoiding unphysically high densities where the two streams collide. This should affect early-stage supersonic refilling, as distinct from late-stage subsonic refilling. While *Rasmussen and Schunk* [1988] state that, "the rate of refilling is not substantially altered by the counterstreaming flow," their Figure 2 suggests that the two-stream treatment may produce a higher early-stage refilling rate than the single-fluid model. The effect of an improved refilling model on the refilling rate is certainly worth revisiting in the context of a global ionosphere-plasmasphere model.

References

Bailey, G. J., and R. Sellek (1990), A mathematical model of the Earth's plasmasphere and its application in a study of He(+) at L = 3, *Ann. Geophys.*, *8*, 171–189.

Baransky, L., J. Borovkov, M. Gokhberg, S. Krylov, and V. Troitskaya (1985), High resolution method of direct measurement of the magnetic field lines' eigen frequencies, *Planet. Space Sci.*, *33*(12), 1369–1374, doi:10.1016/0032-0633(85)90112-6.

Berube, D., M. B. Moldwin, and J. M. Weygand (2003), An automated method for the detection of field line resonance frequencies using ground magnetometer techniques, *J. Geophys. Res.*, *108*(A9), 1348, doi:10.1029/2002JA009737.

Berube, D., M. B. Moldwin, S. F. Fung, and J. L. Green (2005), A plasmaspheric mass density model and constraints on its heavy ion concentration, *J. Geophys. Res.*, *110*, A04212, doi:10.1029/2004JA010684.

Bilitza, D. (1986), International reference ionosphere: Recent developments, *Radio Sci.*, *21*(3), 343–346, doi:10.1029/RS021i003p00343.

Bilitza, D., and B. W. Reinisch (2008), International reference ionosphere 2007: Improvements and new parameters, *Adv. Space Res.*, *42*(4), 599–609, doi:10.1016/j.asr.2007.07.048.

Burch, J. L. (2000), Image mission overview, *Space Sci. Rev.*, *91*, 1–14.

Carpenter, D. L. (1966), Whistler studies of the plasmapause in the magnetosphere: 1. Temporal variations in the position of the knee and some evidence on plasma motions near the knee, *J. Geophys. Res.*, *71*, 693–709.

Chen, L., R. M. Thorne, V. K. Jordanova, C.-P. Wang, M. Gkioulidou, L. Lyons, and R. B. Horne (2010), Global simulation of EMIC wave excitation during the 21 April 2001 storm from coupled RCM-RAM-HOTRAY modeling, *J. Geophys. Res.*, *115*, A07209, doi:10.1029/2009JA015075.

Craven, P. D., D. L. Gallagher, and R. H. Comfort (1997), Relative concentration of He^+ in the inner magnetosphere as observed by the DE 1 retarding ion mass spectrometer, *J. Geophys. Res.*, *102*(A2), 2279–2289, doi:10.1029/96JA02176.

Crowley, G., C. Freitas, A. Ridley, D. Winningham, R. G. Roble, and A. D. Richmond (1999), Next generation space weather specification and forecasting model, in *Proceedings of the 1999 Ionospheric Effects Symposium*, edited by J. M. Goodman, pp. 34–41, JMG Assoc., Alexandria, Va.

Denton, R. E., K. Takahashi, I. A. Galkin, P. A. Nsumei, X. Huang, B. W. Reinisch, R. R. Anderson, M. K. Sleeper, and W. J. Hughes (2006), Distribution of density along magnetospheric field lines, *J. Geophys. Res.*, *111*, A04213, doi:10.1029/2005JA011414.

Denton, R. E., Y. Wang, P. A. Webb, P. M. Tengdin, J. Goldstein, J. A. Redfern, and B. W. Reinisch (2012), Magnetospheric electron density long term (>1 day) refilling rates inferred from passive radio emissions measured by IMAGE RPI during geomagnetically quiet times, *J. Geophys. Res.*, *117*, A03221, doi:10.1029/2011JA017274.

Denton, R. E., K. Takahashi, M. F. Thomsen, J. E. Borovsky, H. J. Singer, Y. Wang, J. Goldstein, P. C. Brandt, and B. W. Reinisch (2014), Evolution of mass density and O^+ concentration at geostationary orbit during storm and quiet events, *J. Geophys. Res. Space Physics*, *119*, 6417–6431, doi:10.1002/2014JA019888.

Drob, D. P., et al. (2008), An empirical model of the Earth's horizontal wind fields: HWM07, *J. Geophys. Res.*, *113*, A12304, doi:10.1029/2008JA013668.

Drob, D. P., et al. (2015), An update to the Horizontal Wind Model (HWM): The quiet time thermosphere, *Earth Space Sci.*, *2*, 301–319, doi:10.1002/2014EA000089.

Emmert, J. T., S. E. McDonald, D. P. Drob, R. R. Meier, J. L. Lean, and J. M. Picone (2014), Attribution of interminima changes in the global thermosphere and ionosphere, *J. Geophys. Res. Space Physics*, *119*, 6657–6688, doi:10.1002/2013JA019484.

Frank, L. A., K. L. Ackerson, W. R. Paterson, J. A. Lee, M. R. English, and G. L. Pickett (1994), The Comprehensive Plasma Instrumentation (CPI) for the GEOTAIL spacecraft, *J. Geomagn. Geoelectr.*, *46*(1), 23–37, doi:10.5636/jgg.46.23.

Galvan, D. A., M. B. Moldwin, and B. R. Sandel (2008), Diurnal variations in plasmaspheric He^+ inferred from extreme ultraviolet images, *J. Geophys. Res.*, *113*, A09216, doi:10.1029/2007JA013013.

Garcia, L. N., S. F. Fung, J. L. Green, S. A. Boardsen, B. R. Sandel, and B. W. Reinisch (2003), Observations of the latitudinal structure of plasmaspheric convection plumes by IMAGE-RPI and EUV, *J. Geophys. Res.*, *108*(A8), 1321, doi:10.1029/2002JA009496.

Goldstein, J., B. R. Sandel, W. T. Forrester, and P. H. Reiff (2003), IMF-driven plasmasphere erosion of 10 July 2000, *Geophys. Res. Lett.*, *30*(3), 1146, doi:10.1029/2002GL016478.

Goldstein, J., M. F. Thomsen, and A. DeJong (2014), In situ signatures of residual plasmaspheric plumes: Observations and simulation, *J. Geophys. Res. Space Physics*, *119*, 4706–4722, doi:10.1002/2014JA019953.

Harten, R., and K. Clark (1995), The design features of the GGS WIND and POLAR spacecraft, *Space Sci. Rev.*, *71*, 23–40, doi:10.1007/BF00751324.

Hedin, A. E. (1987), MSIS-86 thermospheric model, *J. Geophys. Res.*, *92*(A5), 4649–4662, doi:10.1029/JA092iA05p04649.

Hedin, A. E. (1991), Revised global model of thermosphere winds using satellite and ground-based observations, *J. Geophys. Res.*, *96*(A5), 7657–7688, doi:10.1029/91JA00251.

Huba, J. D., and J. Krall (2013), Modeling the plasmasphere with SAMI3, *Geophys. Res. Lett.*, *40*, 6–10, doi:10.1029/2012GL054300.

Huba, J. D., and S. Sazykin (2014), Storm time ionosphere and plasmasphere structuring: SAMI3-RCM simulation of the 31 March 2001 geomagnetic storm, *Geophys. Res. Lett.*, *41*, 8208–8214, doi:10.1002/2014GL062110.

Huba, J. D., G. Joyce, and J. A. Fedder (2000), SAMI2 (Sami2 is another model of the ionosphere): A new low-latitude ionosphere model, *J. Geophys. Res.*, *105*(A10), 23,035–23,053, doi:10.1029/2000JA000035.

Huba, J. D., G. Joyce, and J. Krall (2008), Three-dimensional equatorial spread *F* modeling, *Geophys. Res. Lett.*, *35*, L10102, doi:10.1029/2008GL033509.

Jordanova, V. K., Y. S. Miyoshi, S. Zaharia, M. F. Thomsen, G. D. Reeves, D. S. Evans, C. G. Mouikis, and J. F. Fennell (2006), Kinetic simulations of ring current evolution during the geospace environment modeling challenge events, *J. Geophys. Res.*, *111*, A11S10, doi:10.1029/2006JA011644.

Jordanova, V. K., D. T. Welling, S. G. Zaharia, L. Chen, and R. M. Thorne (2012), Modeling ring current ion and electron dynamics and plasma instabilities during a high-speed stream driven storm, *J. Geophys. Res.*, *117*, A00L08, doi:10.1029/2011JA017433.

Krall, J., and J. D. Huba (2013), SAMI3 simulation of plasmasphere refilling, *Geophys. Res. Lett.*, *40*, 2484–2488, doi:10.1002/GRL.50458.

Krall, J., J. D. Huba, and J. A. Fedder (2008), Simulation of field-aligned H$^+$ and He$^+$ dynamics during late-stage plasmasphere refilling, *Ann. Geophys.*, *26*, 1507–1516, doi:10.5194/angeo-26-1507-2008.

Krall, J., J. D. Huba, R. E. Denton, G. Crowley, and T.-W. Wu (2014), The effect of the thermosphere on quiet time plasmasphere morphology, *J. Geophys. Res. Space Physics*, *119*, 5032–5048, doi:10.1002/2014JA019850.

Lambour, R. L., L. A. Weiss, R. C. Elphic, and M. F. Thomsen (1997), Global modeling of the plasmasphere following storm sudden commencements, *J. Geophys. Res.*, *102*(A11), 24,351–24,368, doi:10.1029/97JA02037.

Lemaire, J., and K. I. Gringauz (1998), *The Earth's Plasmasphere*, Cambridge Univ. Press, New York.

Lockwood, M. (1984), Thermospheric control of the auroral source of O+ ions for the magnetosphere, *J. Geophys. Res.*, *89*(A1), 301–315, doi:10.1029/JA089iA01p00301.

Maynard, N. C., and A. J. Chen (1975), Isolated cold plasma regions: Observations and their relation to possible production mechanisms, *J. Geophys. Res.*, *80*(7), 1009–1013, doi:10.1029/JA080i007p01009.

Newberry, I. T., R. H. Comfort, P. G. Richards, and C. R. Chappell (1989), Thermal He+ in the plasmasphere: Comparison of observations with numerical calculations, *J. Geophys. Res.*, *94*(A11), 15,265–15,276, doi:10.1029/JA094iA11p15265.

Nishida, A. (1966), Formation of plasmapause, or magnetospheric plasma knee, by combined action of magnetospheric convections and plasma escape from the tail, *J. Geophys. Res.*, *71*, 5669–5679, doi:10.1029/JZ071i023p05669.

Park, C. G. (1973), Whistler observations of the depletion of the plasmasphere during a magnetospheric substorm, *J. Geophys. Res.*, *78*(4), 672–683, doi:10.1029/JA078i004p00672.

Picone, J. M., A. Hedin, D. Drob, and A. Aikin (2002), NRLMSISE-00 empirical model of the atmosphere: Statistical comparisons and scientific issues, *J. Geophys. Res.*, *107*(A12), 1468, doi:10.1029/2002JA009430.

Rasmussen, C. E., and R. W. Schunk (1988), Multistream hydrodynamic modeling of interhemispheric plasma flow, *J. Geophys. Res.*, *93*, 14,557–14,565, doi:10.1029/JA093iA12p14557.

Rasmussen, C. E., S. M. Guiter, and S. G. Thomas (1993), Two-dimensional model of the plasmasphere: Refilling time constants, *Planet. Space Sci.*, *41*, 35–43, doi:10.1016/0032-0633(93)90015-T.

Reinisch, B. W. (2000), The radio plasma imager investigation on the IMAGE spacecraft, *Space Sci. Rev.*, *91*, 319–359, doi:10.1023/A:1005252602159.

Richards, P. G., and D. G. Torr (1985), Seasonal, diurnal, and solar cyclical variations of the limiting H+ flux in the Earth's topside ionosphere, *J. Geophys. Res.*, *90*(A6), 5261–5268, doi:10.1029/JA090iA06p05261.

Roble, R. G., and E. C. Ridley (1994), A thermosphere-ionosphere-mesosphere-electrodynamics general circulation model (time-GCM): Equinox solar cycle minimum simulations (30–500 km), *Geophys. Res. Lett.*, *21*(6), 417–420, doi:10.1029/93GL03391.

Scherliess, L., and B. G. Fejer (1999), Radar and satellite global equatorial F region vertical drift model, *J. Geophys. Res.*, *104*(A4), 6829–6842, doi:10.1029/1999JA900025.

Singer, H. J., D. J. Southwood, R. J. Walker, and M. G. Kivelson (1981), Alfven wave resonances in a realistic magnetospheric magnetic field geometry, *J. Geophys. Res.*, *86*(A6), 4589–4596, doi:10.1029/JA086iA06p04589.

Singh, A. K., R. P. Singh, and D. Siingh (2011), State studies of Earth's plasmasphere: A review, *Planet. Space Sci.*, *59*, 810–834, doi:10.1016/j.pss.2011.03.013.

Singh, N., and J. L. Horwitz (1992), Plasmasphere refilling: Recent observations and modeling, *J. Geophys. Res.*, *97*(A2), 1049–1079, doi:10.1029/91JA02602.

Stern, D. P. (1975), The motion of a proton in the equatorial magnetosphere, *J. Geophys. Res.*, *80*(4), 595–599, doi:10.1029/JA080i004p00595.

Stone, E. C., A. M. Frandsen, R. A. Mewaldt, E. R. Christian, D. Margolies, J. F. Ormes, and F. Snow (1998), The advanced composition explorer, *Space Sci. Rev.*, *86*, 1–22, doi:10.1023/A:1005082526237.

Su, Y.-J., M. F. Thomsen, J. E. Borovsky, and D. J. Lawrence (2001), A comprehensive survey of plasmasphere refilling at geosynchronous orbit, *J. Geophys. Res.*, *106*(A11), 25,615–25,629, doi:10.1029/2000JA000441.

Takahashi, K., R. E. Denton, and H. J. Singer (2010), Solar cycle variation of geosynchronous plasma mass density derived from the frequency of standing Alfvén waves, *J. Geophys. Res.*, *115*, A07207, doi:10.1029/2009JA015243.

Tsyganenko, N. A., and M. Sitnov (2005), Modeling the dynamics of the inner magnetosphere during strong geomagnetic storms, *J. Geophys. Res.*, *110*, A03208, doi:10.1029/2004JA010798.

Varney, R. H., W. Swartz, D. Hysell, and J. Huba (2012), SAMI2-PE: A model of the ionosphere including multistream interhemispheric photoelectron transport, *J. Geophys. Res.*, *117*, A06322, doi:10.1029/2011JA017280.

Vellante, M., and M. Förster (2006), Inference of the magnetospheric plasma mass density from field line resonances: A test using a plasmasphere model, *J. Geophys. Res.*, *111*, A11204, doi:10.1029/2005JA011588.

Volland, H. (1973), A semiempirical model of large-scale magnetospheric electric fields, *J. Geophys. Res.*, *78*(1), 171–180, doi:10.1029/JA078i001p00171.

Waters, C. L., F. W. Menk, and B. J. Fraser (1991), The resonance structure of low latitude pc3 geomagnetic pulsations, *Geophys. Res. Lett.*, *18*(12), 2293–2296, doi:10.1029/91GL02550.

Webb, P., R. Benson, R. Denton, J. Goldstein, L. Garcia, and B. Reinisch (2007), An inner magnetospheric electron density database determined from IMAGE/RPI passive dynamic spectra, *Eos Trans. AGU*, *88*(52), Fall Meet. Suppl., Abstract SM12A–04.

Weimer, D. R. (2005), Predicting surface geomagnetic variations using ionospheric electrodynamic models, *J. Geophys. Res.*, *110*, A12307, doi:10.1029/2005JA011270.